LCL Resonance Analysis and Damping in Single-Loop Grid-Forming Wind Turbines

Meng Chen, *Member, IEEE,* Yufei Xi, *Member, IEEE,* Frede Blaabjerg, *Fellow, IEEE,* Lin Cheng, *Senior Member, IEEE,* and Ioannis Lestas, *Member, IEEE*

Abstract—**A dynamic phenomenon known as LCL resonance is often neglected when stability analysis is carried out for grid-forming (GFM) control schemes by wind turbine systems, due to its high frequency. This paper shows that this simplification is not always valid for single-loop (SL) control schemes. A detailed small-signal analysis reveals that reactive power (RAP) control significantly influences the resonant modes, which may be dominant in determining overall system stability, even if the resonant frequency is high. The underlying mechanism via which the LCL resonance may dominate the overall system stability is systematically analyzed. Furthermore, various RAP control strategies are compared to assess their different effects on resonant modes. An active damping (AD) strategy favorable for SL-GFM control is then designed. We also provide a comparison between SL-GFM and well-studied grid-following control schemes, highlighting quite different resonance features between them. Finally, case studies associated with a 14-bus, 5-machine IEEE test system are presented. These show that instability originates from the LCL resonance rather than low-frequency interactions among multiple machines, validating the theoretical analysis and the proposed AD strategy.**

Index Terms—**LCL resonance, single-loop grid-forming control, reactive power control, wind turbines, active damping.**

I. INTRODUCTION

GRID-forming (GFM) permanent magnet synchronous generator (PMSG)-based wind turbines [1]–[3], are classified into multi-loop (ML) [4] and single-loop (SL) structures [5], [6]. ML-GFM include outer power and inner loops [7], while SL-GFM relies only on power control to generate voltage references [8]. Despite sacrificing direct inner voltage and current control, SL-GFM offers simpler implementation and potentially improved small-signal stability [9].

GFM control design can follow two approaches: one optimizes all control loops and couplings together using advanced tuning techniques like H_∞ synthesis [10], [11], while the other decomposes the system into decoupled loops based on reasonable assumptions and design specifications. The

latter approach, allowing for independent tuning of each loop, simplifies the design process and is more commonly used.

In a PMSG-WT system, if the DC voltage is controlled by the machine-side converter (MSC) and GFM control is applied to the grid-side converter (GSC), the DC dynamics, though affected by the AC side, do not impact the AC loops, leading to their decoupling [6], [12]. On the AC side, the active power (AP) and reactive power (RAP) loops can be considered decoupled in an inductive grid [13]. Since power loops are closely linked to angle and synchronization stability, they remain a key focus in GFM converter research, with significant advancements having been reported [11], [14], [15].

A fundamental requirement for accurately representing GFM converter dynamics using low-frequency power loops is ensuring proper frequency separation from other critical frequencies, such as the synchronous frequency and inner loop bandwidths [16]. To achieve such effective decoupling, the AP loop crossover frequency should typically be no more than one-tenth of the synchronous frequency [17]. Otherwise, synchronous frequency resonance must be actively suppressed using methods like physical or virtual resistors or pole elimination [18]. Similarly, coupling between the AP and inner voltage loops can occur in high short-circuit ratio (SCR) systems due to a reduced voltage loop bandwidth [19].

Another critical dynamic phenomenon at higher frequencies is LCL resonance, which has been extensively studied in conventional grid-following (GFL) converters [20], [21]. In GFL converters, both the coupling with the current loop and appropriate active damping (AD) strategies have been thoroughly analyzed [22]–[24]. In contrast, LCL resonance is typically considered negligible in GFM converters, especially in SL-GFM structures. This assumption relies on two main factors: (1) the absence of a high-bandwidth inner current loop in SL-GFM converters, and (2) the slow response of power loops, which are expected to remain decoupled from high-frequency resonance dynamics [25]. However, this assumption has not been rigorously validated. A related study about LCL resonance of GFM converters in [26] mainly examines the influence of the filter capacitor, while many other characteristics remain unclear and have not been thoroughly investigated.

This paper provides a comprehensive analysis of LCL resonance in SL-GFM converters, mainly with droop-I RAP control [11]. Considering GFM converters associated with PMSG-WTs as an example, we demonstrate that the dynamic effects of LCL resonance may not be negligible, even when the resonant frequency is relatively high. The key contributions of this paper are summarized as follows:

1) A detailed small-signal analysis is conducted, revealing that RAP control significantly influences the LCL resonance modes, potentially making them the dominant factor in the overall system stability even when the resonant frequency is high. The underlying mechanism through which LCL resonance modes (rather than the power modes) dominate the overall system stability, is systematically analyzed.

2) Various RAP control strategies are compared to evaluate their distinct effects on LCL resonant modes, providing insights for the impact on system stability and dynamics.

3) An AD strategy utilizing capacitor voltage feedback is designed to enhance the stability of SL-GFM control. While a similar AD strategy has been previously applied in GFL converters [27], its benefits and design in the context of SL-GFM converters have not been thoroughly investigated. This paper provides a detailed analysis and justification for its implementation in SL-GFM control.

4) A comparison between SL-GFM and the well-studied GFL control is presented, highlighting significant differences in their resonance behavior and corresponding AD design. This provides valuable insights for the distinct features associated with LCL resonance and damping in various control schemes.

Moreover, a 14-bus, 5-machine IEEE system is used to show that instability can arise from LCL resonance rather than low-frequency interactions among multiple machines, and to validate the underlying resonance behaviour and damping. The Matlab/Simulink implementation is available online [28].

The remainder of the paper is organized as follows: Section II presents a comprehensive small-signal analysis of the SL-GFM converter, emphasizing the significance of LCL resonance and evaluating different RAP control strategies. Section III details the AD design methodology in SL-GFM converters. Section IV summarizes a comparison with GFL converters. Section V provides simulation results, while Section VI summarizes the key findings and conclusions.

II. HIGH-FREQUENCY RESONANCE IN SINGLE-LOOP GRID-FORMING CONVERTERS

A. Structure Description and Conventional Simplified Model

Fig. 1 shows the structure of a PMSG-WT system with an LCL filter, where L_f is the inverter-side filter inductor and C_f is the filter capacitor. The grid-side filter inductor is included into the line inductor L_g, while R_g is the line resistance. The DC voltage control and SL-GFM control are implemented in the MSC and GSC, respectively, as shown in Fig. 2. Control and modeling variables are represented in p.u. values.

On the DC side, the DC-link voltage is regulated by a proportional-integral (PI) controller, as shown below:

$$i_{wdcrf} = k_{pdc}(V_{dcst} - v_{dc}) + k_{idc} \int (V_{dcst} - v_{dc}) dt \quad (1)$$

$$\dot{v}_{dc} = (\omega_n/C_{dc})i_{wdc} - (\omega_n/C_{dc})i_{dc} \quad (2)$$

where i_{wdc} and i_{wdcrf} are the DC current from the MSC and its reference from the PI controller, respectively, k_{pdc} and k_{idc} are the PI controller gains, v_{dc} is the DC-link voltage, the subscript

"st" represents set-point value, C_{dc} is the DC-link capacitor, ω_n is the nominal angular frequency, and i_{dc} is the DC current to the GSC. By simplifying the MSC as a controlled current source, it is assumed that $i_{wdcref} = i_{wdc}$ [11].

On the AC side, the SL-GFM with droop-I RAP control derives voltage references with magnitude E_{rf} and angle θ:

$$2H\dot{\omega} = P_{st} - p - D_p(\omega - \omega_{st}) \quad (3)$$

$$\dot{\theta} = \omega_n\omega \quad (4)$$

$$(1/k_q)\dot{E}_{rf} = Q_{st} - q + D_q(V_{st} - V) \quad (5)$$

where ω is the angular frequency provided by the GFM control, D_p and D_q are the droop coefficients, H and k_q reflect the inertia of the AP and RAP loops, respectively, p, q, and V are the output active power, reactive power, and voltage magnitude measured from the filter capacitor, respectively, which are calculated in dq reference frame oriented by θ as

$$p + jq = (v_d + jv_q)(i_{gd} - ji_{gq}) \quad (6)$$

$$V = \sqrt{v_d^2 + v_q^2} \quad (7)$$

where v and i_g denote the capacitor voltage and line current, the subscripts "d" and "q" represent the d-axis and q-axis components. The active power set-point is determined by the maximum power point tracking (MPPT) control as [6]:

$$P_{st} = (1/2)\rho\pi R^2 C_{opt}(\omega_r^3 R^3)/\lambda_{opt}^3 \quad (8)$$

where ρ is the air density, R is the wind turbine blade length, C_{opt} and λ_{opt} are the optimal power coefficient and optimal tip speed ratio, respectively. Meanwhile, the AC dynamics are coupled to the DC side via the power balance, expressed as

$$v_{dc}i_{dc} = E_{rf}i_d \quad (9)$$

where i is the GSC output current. Thus, the small-signal block diagram of the system can be derived as shown in Fig. 3.

Neglecting the dynamic effects of the LCL filter, simplified static models are given by

$$G_{dcv}(s) := -E_{rf0}i_{d0}/v_{dc0}^2 \quad (10)$$

$$G_{p\delta}(s) := (E_{rf0}V_g/X_{eq})\cos\delta_0 \quad (11)$$

$$G_{qE}(s) := [2E_{rf0}X_g + V_g\cos\delta_0(2X_f - X_{eq})]/X_{eq}^2 \quad (12)$$

$$G_{VE}(s) := \frac{X_g(E_{rf0}X_g + V_gX_f\cos\delta_0)}{X_{eq}\sqrt{E_{rf0}^2X_g^2 + 2E_{rf0}V_gX_fX_g\cos\delta_0 + V_g^2X_f^2}} \quad (13)$$

where the subscript "0" denotes the steady-state value, V_g is the grid voltage magnitude and δ is the angle difference between voltages of GSC and grid, expressed by

$$\dot{\delta} = \omega_n(\omega - \omega_g) \quad (14)$$

where ω_g is the grid angular frequency. Meanwhile, we have $X_{eq} := X_f + X_g - X_cX_fX_g$, where X_f, X_g, and X_c represent the synchronous reactances of the inverter-side inductor, filter capacitor, and line inductor, respectively. Furthermore, neglecting the loop coupling leads to simplified open-loop transfer functions (TFs) for the DC loop, AP loop, and RAP loop expressed as

$$G_{dc\_sim}(s) := \left(k_{pdc} + \frac{k_{idc}}{s}\right)\frac{\omega_n}{C_{dc}s + \omega_nG_{dcv}(s)} \quad (15)$$
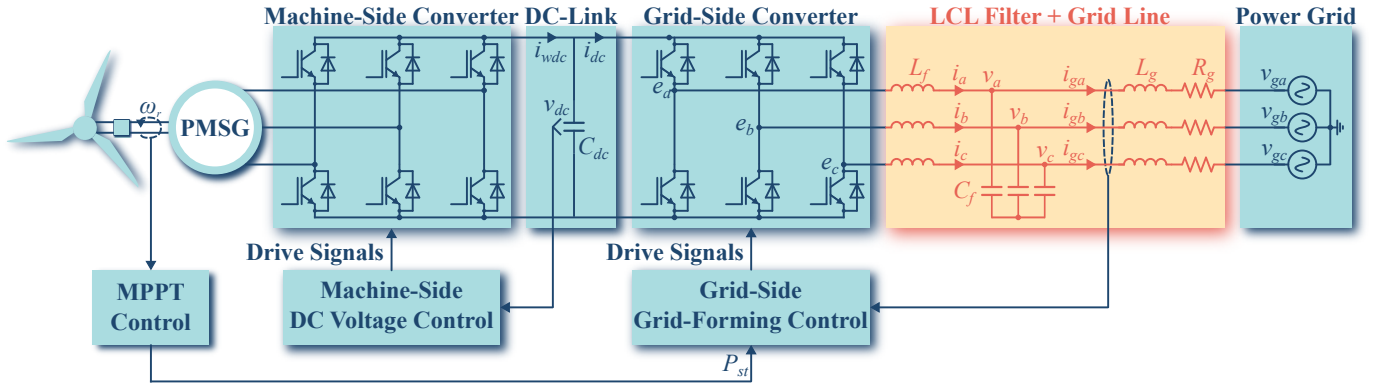
Fig. 1. Structure of a PMSG-WT system with LCL filter controlled by SL-GFM control strategy.
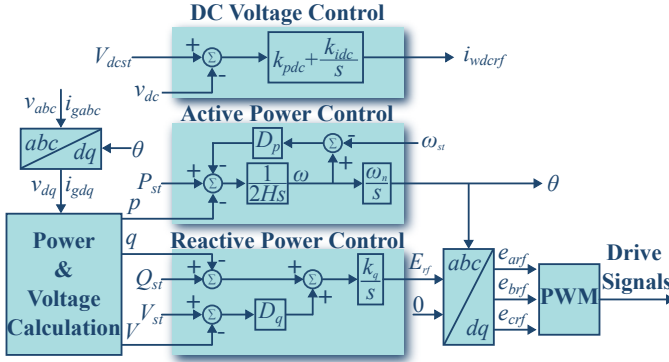

Fig. 2. Detailed control block diagram of PMSG-WT system with droop-I RAP control.
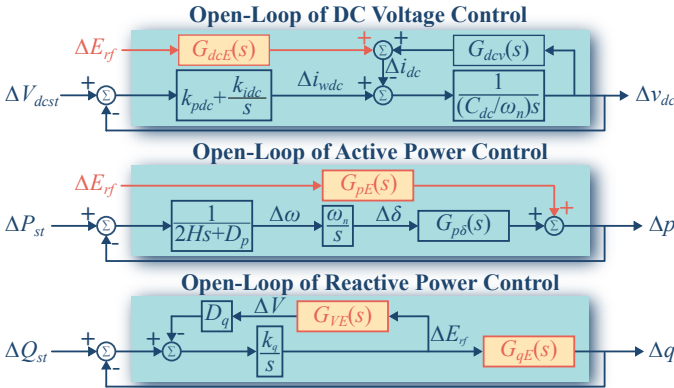

Fig. 3. Small-signal block diagram of SL-GFM PMSG-WT system.

$$G_{p\_sim}(s) := \frac{1}{2Hs + D_p} \frac{\omega_n}{s} G_{p\delta}(s) \qquad (16)$$

$$G_{q\_sim}(s) := G_{qE}(s)/[(1/k_q)s + D_q G_{VE}(s)] \qquad (17)$$

Conventionally, GFM control analysis uses simplified and decoupled open-loop models (15)-(17) for each loop. With the parameters in Table I, their step responses are compared with a simulation of the detailed model, where V_{dcst}, P_{st}, and Q_{st} step 0.05 p.u. at $t = 1$ s, 0.3 p.u. at $t = 2$ s, and 0.1 p.u. at $t = 3$ s, from 1 p.u., 0.5 p.u., and 0 p.u., as shown in Fig. 4. The responses of the simplified models seem to closely match the simulation dynamics with the detailed model. However, in the next section we will show using the detailed model that

TABLE I
PARAMETERS OF SL-GFM PMSG-WT SYSTEM

| Parameters	Description	Values
S_n	Nominal power	5 MW (1 p.u.)
V_n	Nominal line-to-line RMS voltage	690 V (1 p.u.)
f_n	Nominal frequency	50 Hz (1 p.u.)
V_{dcn}	Nominal DC voltage	1200 V (1 p.u.)
f_{sw}	Switching frequency	5 kHz
C_f	Filter capacitor	1.6 mF (0.048 p.u.)
L_f	Inverter-side filter inductor	32 μH (0.1 p.u.)
L_g	Grid-side filter inductor + line	60 μH (0.2 p.u.)
X_g/R_g	X/R ratio of the line	6
C_{dc}	DC-link capacitor	0.3 F (27 p.u.)
H	Inertia constant	0.5 s
D_p	Damping of active power control	50
D_q	Droop coefficient of $q - V$ control	10
k_q	Integral gain of $q - V$ control	4
ω_{st}	Set-point of angular frequency	1 p.u.
Q_{st}	Set-point of reactive power	0 p.u.
V_{st}	Set-point of voltage magnitude	1 p.u.
V_{dcst}	Set-point of DC-link voltage	1 p.u.
k_{pdc}	Proportional gain of DC voltage PI	3.8
k_{idc}	Integral gain of DC voltage PI	63.8
ρ	Air density	1.2 kg/m^3
R	Wind turbine blade length	63 m
C_{opt}	Optimal power coefficient	0.44
λ_{opt}	Optimal tip speed ratio	7
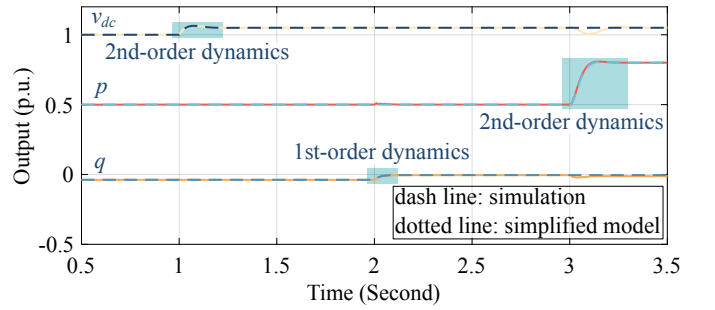
Fig. 4. Comparison of step responses between simplified small-signal model and detailed model of time-domain simulation.

Fig. 4 may be misleading by revealing that:
1) The system exhibits a small stability margin dominated by LCL resonance modes and is prone to instability, a behavior not captured by the simplified model.
2) RAP control is intrinsically coupled with the LCL resonance modes, limiting the ability to freely tune the RAP dynamics as assumed in the simplified model.
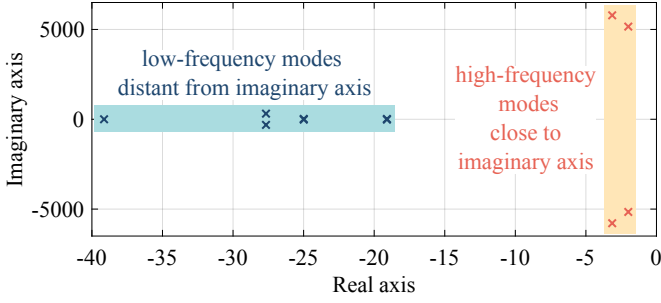
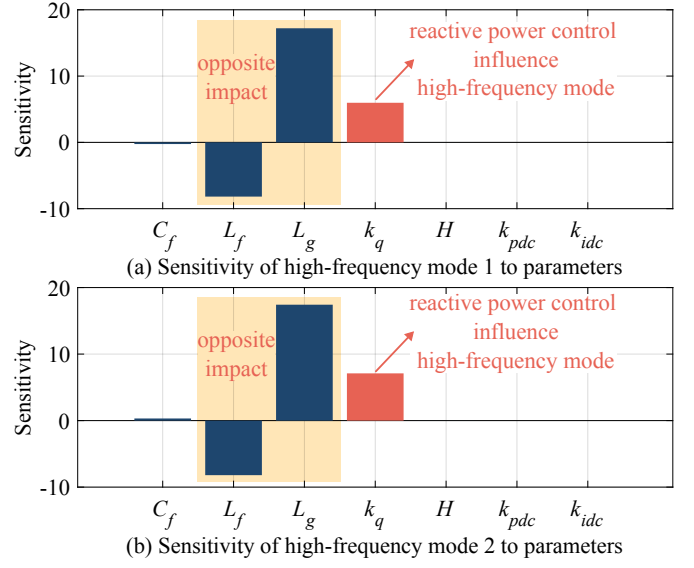Fig. 5. Eigenvalues of detailed model of SL-GFM PMSG-WT system.

Fig. 6. Sensitivity evaluating variation of real parts of resonance modes in response to percentage changes in system parameters.
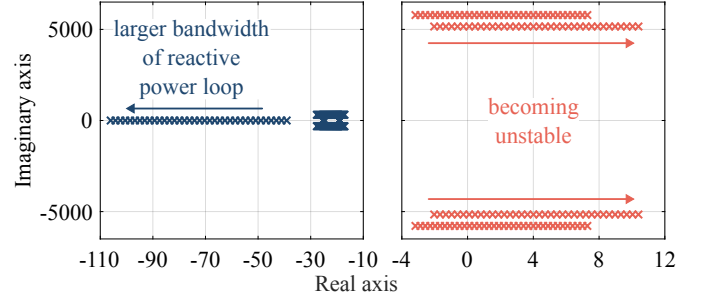

Fig. 7. Root loci when k_q increases from 4 to 11 with corresponding bandwidth of RAP loop increasing from 6 Hz to 17 Hz.

B. Detailed Model with High-Frequency Dynamics

To reflect the high-frequency responses, detailed models of the filter and line are considered, which are expressed as

$$(L_f/\omega_n)\dot{i}_d = E_{rf} - v_d + \omega L_f i_q \tag{18}$$

$$(L_f/\omega_n)\dot{i}_q = -v_q - \omega L_f i_d \tag{19}$$

$$(C_f/\omega_n)\dot{v}_d = i_d - i_{gd} + \omega C_f v_q \tag{20}$$

$$(C_f/\omega_n)\dot{v}_q = i_q - i_{gq} - \omega C_f v_d \tag{21}$$

$$(L_g/\omega_n)\dot{i}_{gd} = v_d - V_g\cos\delta - R_g i_{gd} + \omega L_g i_{gq} \tag{22}$$

$$(L_g/\omega_n)\dot{i}_{gq} = v_q + V_g\sin\delta - R_g i_{gq} - \omega L_g i_{gd}. \tag{23}$$

By combining (1)–(7), (9), (14), and (18)–(23), the detailed system model is formulated, with its eigenvalues shown in Fig. 5. The step responses in Fig. 4 are primarily influenced by low-frequency modes, which are located far from the imaginary axis, indicating a large stability margin. It is noted that Fig. 5 also presents two resonance modes, whose dynamics are not captured in the simplified small-signal model nor observed in the time-domain simulation due to their high frequency. However, these high-frequency modes are located close to the imaginary axis, suggesting a small stability margin and potential risk of instability under minor parameter variations.

A sensitivity [29] analysis is conducted to evaluate the variation of the real parts of the resonance modes in response to percentage changes in system parameters. The results, presented in Fig. 6, show that the AP control and DC voltage control are decoupled with the resonance modes, aligning with conventional expectations. More importantly, Fig. 6 reveals two key observations:

1) Apart from the LCL filter parameters, RAP control significantly affects the high-frequency modes, challenging conventional assumptions.
2) The inverter-side and line inductors L_f and L_g have opposite effects. This behavior differs from GFL converters, where stability depends only on the LCL resonant frequency, and L_f and L_g contribute in similar ways.

To further elaborate the aforementioned observations, a root locus analysis is performed. Fig. 7 shows the root locus diagram as k_q increases from 4 to 11, where the RAP mode shifts from -39 to -106, corresponding to a bandwidth increasing from 6 Hz to 17 Hz. Simultaneously, the resonance modes gradually move to the right-half plane (RHP), making the whole system unstable. This implies that LCL resonance limits the bandwidth of the RAP loop.

Fig. 8 and Fig. 9 show the root loci as L_g increases from 0.2 p.u. to 0.5 p.u and L_f increases from 0.1 p.u. to 0.2 p.u., respectively. As shown, a larger L_g, which implies a weaker grid, increases the damping ratio of the AP loop, aligning with the conventional understanding that GFM control performs better in weak grids [14]. However, it is also observed that the resonance modes move into the RHP, leading to system instability with undamped high-frequency oscillations. This demonstrates that LCL resonance fundamentally constrains the stable operation of SL-GFM converters in weak grids. Conversely, increasing L_f enhances the stability of the resonance modes, pushing them further into the left-half plane (LHP), as shown in Fig. 9. This indicates that L_f and L_g have opposite effects on stability in SL-GFM converters, in contrast to their symmetrical role in GFL converters.

Moreover, the DC loop and the AP loop are actually influenced by the RAP loop through the coupling terms $G_{dcE}(s)$ and $G_{pE}(s)$, as shown in Fig. 3. Consequently, a high-frequency unstable RAP loop is expected to destabilize both the DC and AP loops.

C. Mechanism Analysis

This section analyzes the mechanism by which resonance modes cannot be simply neglected through frequency separa-
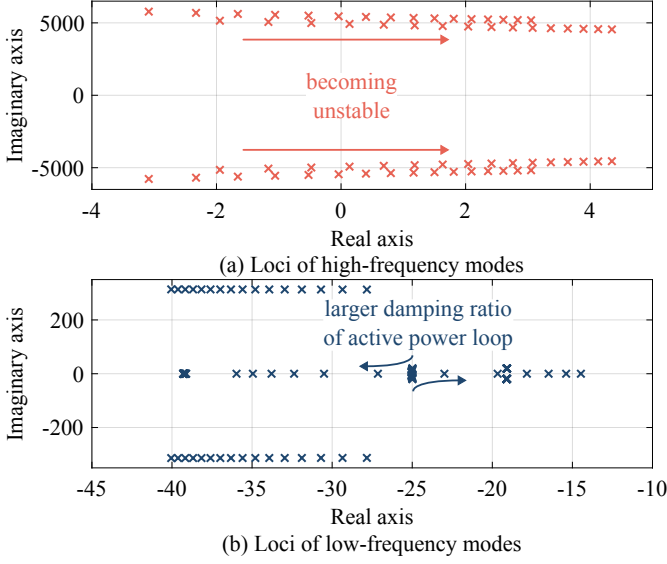
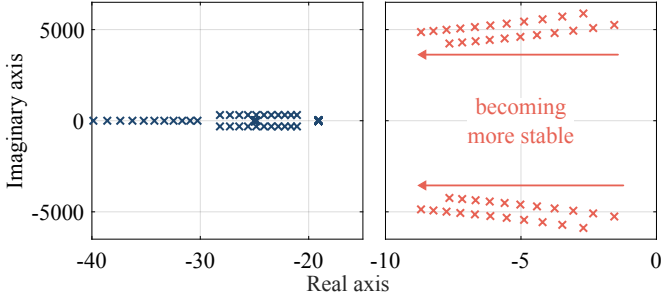Fig. 8. Root loci when L_g increases from 0.2 p.u. to 0.5 p.u.

Fig. 9. Root loci when L_f increases from 0.1 p.u. to 0.2 p.u.

tion and why they play a crucial role in the overall stability of the SL-GFM converter.

The findings in Section II-B suggest a need for further analysis of the RAP loop using the detailed model. Assuming $R_g = 0$ for the worst case, the TFs related to the RAP loop in Fig. 3, (12) and (13), should be reformulated as:

$$G_{qE}(s) := N_{qE}(s)/[(s^2 + \omega_n^2\omega_g^2)D_{LCL}(s)] \quad (24)$$

$$G_{VE}(s) := N_{VE}(s)/D_{LCL}(s) \quad (25)$$

where

$$N_{qE}(s) := \frac{\omega_n^2}{L_f L_g C_f}[v_{q0}(s^3 + \omega_n^2\omega_{res}^2 s - 3\omega_n^2\omega_g^2 s)$$
$$- v_{d0}(\omega_n^3\omega_g^3 - \omega_n^3\omega_{res}^2\omega_g - 3\omega_n\omega_g s^2)$$
$$- i_{gq0}L_g(s^2 + \omega_n^2\omega_g^2)(s^2 + \omega_n^2\omega_{res}^2 - \omega_n^2\omega_g^2)$$
$$- 2i_{gd0}L_g\omega_n\omega_g s(s^2 + \omega_n^2\omega_g^2)] \quad (26)$$

$$N_{VE}(s) := \frac{\omega_n^2}{L_f C_f V_0}[v_{d0}(s^2 + \omega_n^2\omega_{res}^2 - \omega_n^2\omega_g^2) - 2v_{q0}\omega_n\omega_g s] \quad (27)$$

$$D_{LCL}(s) := [s^2 + \omega_n^2(\omega_{res} + \omega_g)^2][s^2 + \omega_n^2(\omega_{res} - \omega_g)^2] \quad (28)$$

and ω_{res} is the LCL resonant frequency defined as [23]:

$$\omega_{res} := \sqrt{(L_f + L_g)/(L_f L_g C_f)} \quad (29)$$

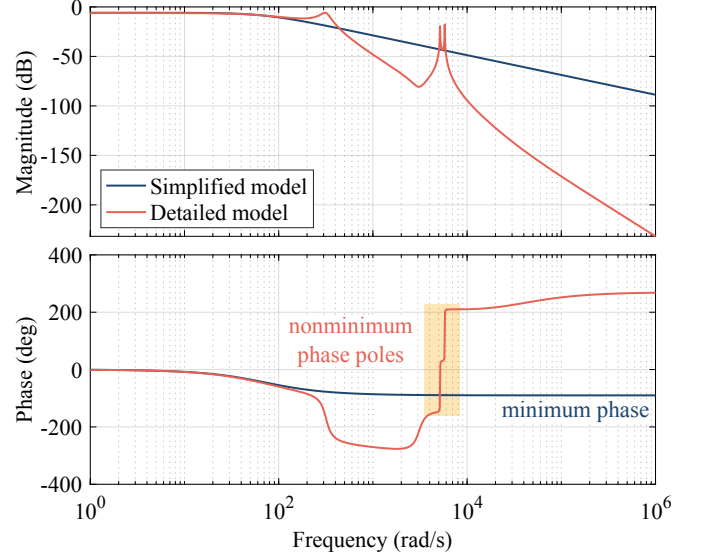| Open-loop Poles	Modes	Characteristics
$7.8 \pm j5785.2$	LCL resonance	nonminimum
$9.9 \pm j5159.9$		phase (unstable)
$-34.3 \pm j316.2$	synchronous resonance	minimum phase
-71.6	RAP control	(stable)

Fig. 10. Comparison of open-loop Bode plots of RAP loops using simplified model and detailed model when $k_q = 11$.

Finally, the open-loop TF of the RAP loop with the detailed model can be derived as

$$G_q(s) := \frac{k_q N_{qE}(s)}{[sD_{LCL}(s) + k_q D_q N_{VE}(s)](s^2 + \omega_n^2\omega_g^2)} \quad (30)$$

where its poles are calculated in Table II supposing k_q increases to 11. Beyond all other poles located in the LHP, four RHP poles corresponding to resonance frequencies are observed. This indicates that the open-loop RAP loop behaves as a nonminimum phase system, as also reflected in the open-loop Bode plot of Fig. 10. In this figure, the simplified model aligns with the detailed model at low frequencies. Nevertheless, using the Bode plots to assess system stability without taking into account the presence of open-loop unstable poles is inappropriate [29]. Although Fig. 10 indicates positive stability margins when considering only the 0 dB magnitude and $-180°$ phase crossover criteria, the system is actually unstable in our case according to the previous root loci of Fig. 7, or if one uses the full Nyquist criterion with the open loop unstable poles taken into consideration. While the impact of nonminimum phase on synchronous frequency resonance has been studied in [18], this paper highlights that LCL resonance plays a more critical role in the studied SL-GFM converter rather than the synchronous frequency resonance.

D. Comment on Different $q - V$ Control Strategies

This section compares the resonance behavior of SL-GFM converters under six different RAP controls, given the significant influence of RAP control on resonance modes. Fig.
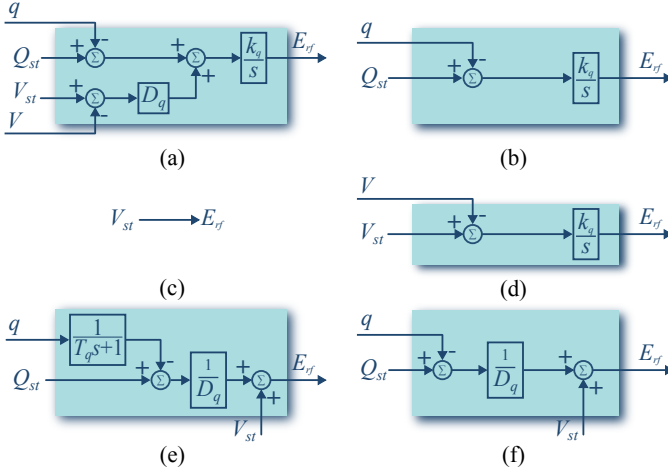
Fig. 11. Typical RAP control structures illustrated for comparison. (a) Droop-I control; (b) RAP control; (c) Fixed voltage control; (d) Voltage control; (e) Droop control; (f) Pure droop control.
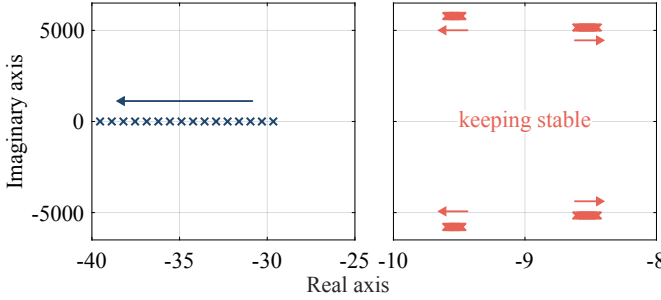

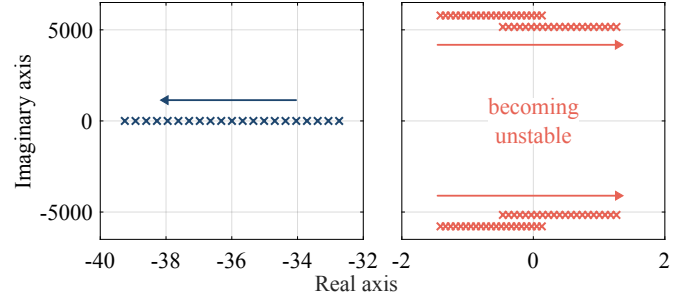Fig. 12. Root loci of SL-GFM converter with RAP control as in Fig. 11(b).

Fig. 13. Root loci of SL-GFM converter with voltage control as in Fig. 11(d).
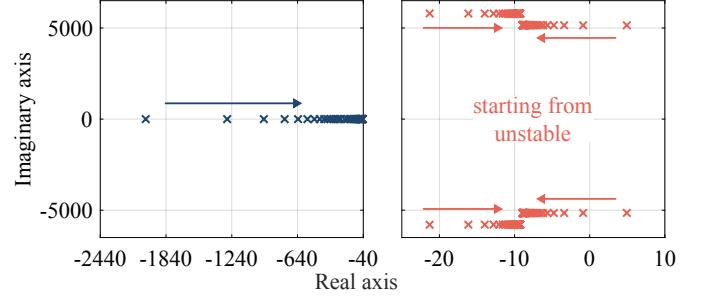
Fig. 14. Root loci of SL-GFM converter with droop control as in Fig. 11(e)

11 summarizes the considered control structures: (a) droop-I control, used in the previous sections and as a reference for the comparison; (b) RAP control (without droop characteristics); (c) fixed voltage control; (d) voltage control; (e) droop control [19]; and (f) pure droop control (without a power filter) [4]. Meanwhile, for a fair comparison, all corresponding RAP modes are adjusted to about -40, consistent with Fig. 5. Only the RAP mode and resonance modes are shown in this Section.

1) RAP Control: Its mode can be adjusted via the integral gain, with the corresponding root loci shown in Fig. 12. The results indicate that changes in RAP bandwidth have minimal impact on the resonance modes. When the RAP mode is positioned at -40, the resonance modes shift further away from the imaginary axis compared to Fig. 5, suggesting improved system stability.

2) Fixed Voltage Control: The inverter voltage is directly assigned without regulation, equivalent to Fig. 11(b) with $k_q = 0$. Referring to Fig. 12 and considering a gradual reduction of k_q to zero, the critical resonance mode will move to the left. This indicates improved stability compared to RAP control.

3) Voltage Control: Its mode can also be tuned via the integral gain, with the corresponding root loci presented in Fig. 13. The results indicate that increasing voltage regulation speed adversely affects the stability of the resonance modes. As the low frequency mode moves to -40, the resonance modes shift into the RHP, rendering the system unstable. This suggests that its resonance stability is worse than that of the

droop-I control.

4) Droop Control: Its mode can be adjusted via the time constant of the RAP filter T_q, with the corresponding root loci shown in Fig. 14. The results indicate that T_q has opposite effects on the two resonance modes, with the critical mode gradually shifting from the RHP to the LHP, improving system stability. When the RAP mode reaches -40, the critical resonance mode is positioned farthest in the LHP compared to all previously discussed strategies, suggesting that this approach provides the best stability properties for the resonance modes.

5) Pure Droop Control: The RAP q is directly fed back to the droop mechanism without a pre-filter, which corresponds to Fig. 11(e) with $T_q = 0$. As observed in Fig. 14, a small T_q results in unstable resonance modes. Therefore, pure droop control cannot be directly applied to SL-GFM converters unless the resonance effects are properly mitigated.

In summary, the resonance stability of various RAP control structures in Fig. 11 can be ranked as

$$\underbrace{(e) > (c) > (b) > (a) > (d)}_{\text{Stable or could be tuned to be stable}} > \underbrace{(f)}_{\text{Unstable}}$$

III. ACTIVE DAMPING STRATEGY FOR HIGH-FREQUENCY RESONANCE

A. Selection of Active Damping Implementation

This section explores an appropriate active damping (AD) strategy for SL-GFM converters to mitigate LCL resonance. Ideally, AD introduces a virtual resistor in one of six possible locations, labeled R_{v1} to R_{v6} in Fig. 15. As discussed in [24], all virtual resistors can be implemented using feedback from i_{abc}, i_{gabc}, i_{cabc}, or v_{abc}, leading to 24 possible AD configurations. For GFL converters, i_{gabc} feedback to implement R_{v4} has been identified as the most suitable approach in terms of
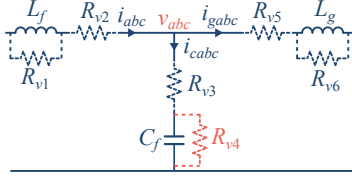
Fig. 15. Equivalent virtual resistors of various AD strategies.

Fig. 16. Relationship between coupling strength K_{qp} and negative real part of critical resonance mode using different virtual resistors.

number of sensors, implementation complexity, and damping effectiveness. However, applying these same selection criteria to SL-GFM converters leads to a different optimal choice, as will be discussed in this section.

1) Number of Sensors: For SL-GFM converters, both i_{gabc} and v_{abc} are measured for power calculation. Therefore, the AD should be implemented using only these variables whenever possible, avoiding additional sensors. This requirement leads to 12 possible implementations.

2) Complexity: Using i_{gabc} results in controllers where the order of the numerator is higher by at least two than that of the denominator. The same applies when constructing R_{v1}, R_{v3}, or R_{v6} with v_{abc} [24]. These choices are not favorable in practice due to implementation complexity. Consequently, only three viable options remain: using v_{abc} to construct R_{v2}, R_{v4}, or R_{v5}. Notably, while i_{gabc} is preferred in GFL converters, it is recognized as not being the most suitable approach for SL-GFM converters at this stage.

3) Effectiveness: The added AD should minimize its negative impact on the original system. In GFL converters, the primary concern is whether the damped resonance limits the current loop bandwidth. However, this is not a concern for SL-GFM converters. Instead, a key issue in GFM converters is the coupling between AP and RAP loops. This paper evaluates the coupling strength by analyzing the steady-state change in RAP caused by an AP step, defined as:

$$K_{qp} := \lim_{s \to 0} \frac{\Delta q(s)}{\Delta P_{st}(s)} \quad (31)$$

where its relationship with the negative real part of the critical resonance mode using different virtual resistors is shown in Fig. 16. The results indicate that a more stable resonance mode leads to stronger coupling when using R_{v5}. In contrast, R_{v2} and R_{v4} do not affect the coupling strength, making them more favorable choices. These observations can be explained using the system steady-state equations, expressed as

$$P_{st} - p - D_p(\omega - \omega_{st}) = 0 \quad (32)$$

$$Q_{st} - q + D_q(V_{st} - V) = 0 \quad (33)$$

$$p = \frac{V^2 R_g + V V_g(X_g \sin \delta_v - R_g \cos \delta_v)}{R_g^2 + X_g^2} \quad (34)$$

$$q = \frac{V^2 X_g - V V_g(R_g \sin \delta_v + X_g \cos \delta_v)}{R_g^2 + X_g^2} \quad (35)$$

where δ_v represents the angle difference between v_{abc} and V_{gabc}, and the solution vector of $[p \ q \ V \ \delta_v]$ can be uniquely determined. Clearly, these steady-state equations are independent of R_{v2} and R_{v4}, whereas R_{v5} increases R_g, strengthening the coupling.
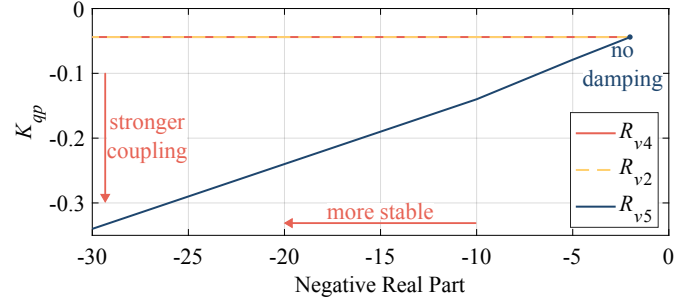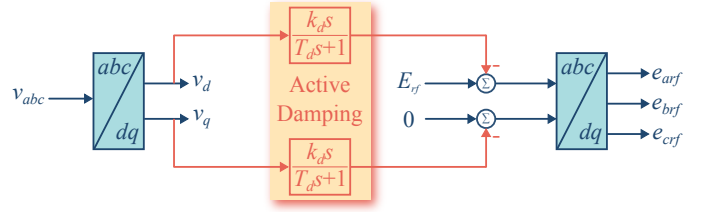

Fig. 17. Block diagram of AD strategy for SL-GFM converters.

As a result, implementing capacitor voltage feedback to construct R_{v2} or R_{v4} is the preferred approach for SL-GFM converters. The corresponding AD controllers are defined as:

$$G_{ad}(s) := \begin{cases} k_d s + k_i/s & \text{for } R_{v2} \\ k_d s & \text{for } R_{v4} \end{cases} \quad (36)$$

where k_d and k_i are parameters to be designed, and R_{v4} is chosen so as to have a simple implementation in practice. It is noted that a similar AD strategy based on v_{abc} has been previously applied in GFL converters [27]. Nevertheless, its benefits and design in the context of SL-GFM converters has not been reported or analyzed in the literature.

B. Design of Active Damping

Based on (36), the favorable AD is implemented by feeding back v_{abc} through a first-order derivative element. In practice, it is realized as:

$$G_{ad}(s) := \frac{k_d s}{T_d s + 1} \quad (37)$$

where T_d is a time constant. Finally, the implemented AD strategy in the dq reference frame is shown in Fig. 17.

The following paragraph presents a step-by-step design procedure for $G_{ad}(s)$, based on the analysis in the previous sections:

- *Step 1*: Determine specifications in terms of the placement of the RAP mode and L_g. As shown in Section II-B, a RAP mode farther from the imaginary axis and a larger L_g increase the likelihood of instability in the resonance modes. Therefore, $G_{ad}(s)$ can be designed based on the worst-case scenario, where the RAP mode is placed at the farthest distance and L_g takes its largest value. This ensures robustness for all actual RAP modes and L_g values within those maximum values. This approach is
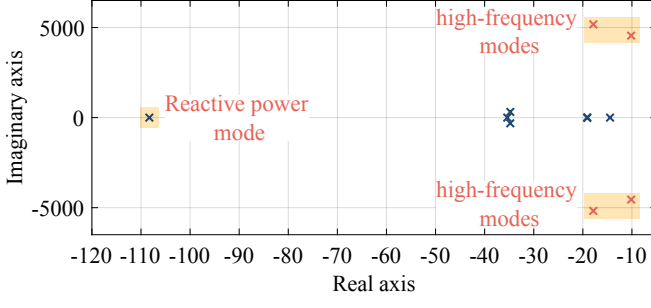
Fig. 18. Designed eigenvalues based on worst-case scenario.

illustrated in this paper by requiring the resonance to be damped when the RAP mode is placed at about -110, corresponding to 17 Hz, with L_g set to 0.5 p.u., which corresponds to a SCR of 2.

- *Step 2*: Determine the stability margin in terms of the resonance modes. In this paper, as an example, the requirement is that the negative real part of the critical resonance mode must be less than -10 to ensure a sufficient stability margin.

- *Step 3*: Determine k_d via small-signal analysis. This step assumes $T_d = 0$ and results in $k_d = 3.3 \times 10^{-6}$. The system eigenvalues, shown in Fig. 18, confirm that the placement meets the defined specifications and stability margin. Notably, the small-signal analysis is conducted under the worst-case scenario defined in *Step 1*, and thus an exact line impedance value is unnecessary.

- *Step 4*: Determine T_d. T_d is introduced to avoid pure derivative action without significantly affecting the desired transfer function characteristics at the resonant frequency. It is set to $T_d = 8 \times 10^{-5}$, ensuring a breakpoint frequency of 2 kHz, which is twice the designed LCL resonant frequency. Finally, $G_{ad}(s)$ is designed as:

$$G_{ad}(s) = \frac{3.3 \times 10^{-6} s}{8 \times 10^{-5} s + 1} \quad (38)$$

- *Step 5*: Validation.

IV. COMPARISON OF LCL RESONANCE BETWEEN GFL AND SL-GFM CONVERTERS

LCL resonance and its damping strategies have been extensively studied in GFL converters. Therefore, this section summarizes the findings in the previous sections and provides a comparison between SL-GFM (with droop-I RAP control) and GFL converters, highlighting their distinct characteristics in relation to LCL resonance and damping. The key features are compared in Table III.

- *Power Stage*: In both GFL and SL-GFM converters, LCL filter parameters naturally affect resonance. However, in GFL converters, the resonant frequency is the primary concern, with L_f and L_g having identical effects [22], [23]. In contrast, L_f and L_g have opposite impact on the resonance modes in SL-GFM converters.

- *Control*: In GFL converters, resonance stability primarily depends on current control and can be assessed using root

TABLE III
COMPARISON OF LCL RESONANCE BETWEEN SL-GFM AND GFL CONVERTERS

		SL-GFM Converter	GFL Converter
Power stage	Critical parameters	L_f, C_f, L_g	L_f, C_f, L_g
	Roles of L_f and L_g	**Opposite**	**Identical**
Control	Measured variables	Grid currents **Capacitor voltages**	Grid currents
	Critical loops	**RAP control**	**Current control**
	Open-loop system	**May become Nonminimum phase**	**Minimum phase**
	Stability Analysis	Root loci Nyquist criterion	Root loci Nyquist criterion **Bode plot**
Selected AD	Selection criteria	number of sensors Complexity **Bandwidth**	number of sensors Complexity **Coupling strength**
	Virtual resistor	Paralleled with C_f	Paralleled with C_f
	Feedback variables	**Capacitor voltages**	**Line currents**

loci for the closed-loop system or frequency responses (Nyquist and Bode plots) for open-loop minimum phase systems. In contrast, the critical loop in SL-GFM converters is the RAP control. Since the SL-GFM's open-loop system may become nonminimum phase/unstable, the Bode plot for evaluating stability margins needs to be carefully used in conjunction with any open-loop unstable poles present. Additionally, SL-GFM control uses both grid current and capacitor voltage measurements for power calculation, enabling more flexible AD implementations without extra sensors than GFL converters, which rely only on grid current.

- *Selected AD*: AD for both GFL and SL-GFM converters can be selected using similar criteria. However, in GFL converters, AD effectiveness should not compromise control bandwidth whenever possible, whereas in SL-GFM converters, minimizing the coupling between AP and RAP loops is more critical. As results from the AD selection criteria discussed, line current feedback is preferred for GFL converters [23], [24], while capacitor voltage feedback is more suitable for SL-GFM converters. Despite this difference, the optimal placement of the virtual resistor in both cases is recognized as being parallel to the filter capacitor.

V. TEST CASES

Various case studies are presented in this section that demonstrate that instability originates from LCL resonance rather than low-frequency interactions among multiple machines, thus verifying the analysis and the effectiveness of the proposed AD. The case studies are associated with a 14-bus, 5-machine IEEE Test System [30] as shown in Fig. 19. An SL-GFM controlled PMSG-WT system is connected to Bus 6, where the parameters are the same as those in Table I, unless otherwise specified. The Matlab/Simulink implementation of this paper is available online [28].
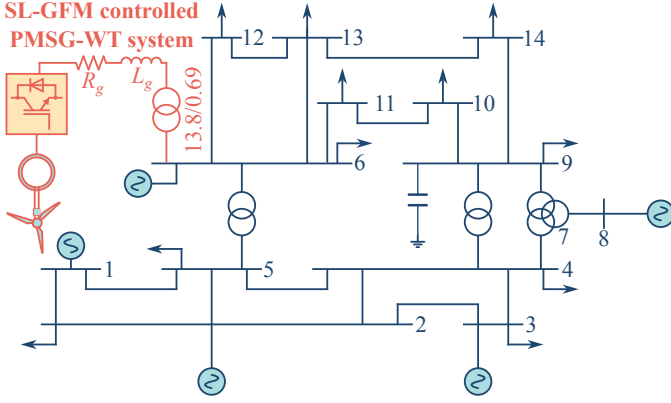
Fig. 19. 14-bus system diagram with SL-GFM controlled PMSG-WT system.

Using the parameters in Table I, simulation results for the DC-link voltage v_{dc}, output AP p, and output RAP q are shown in Fig. 20. Initially, the system has a stable behaviour. At $t = 5$ s, k_q is increased from 4 to 18 to raise the bandwidth corresponding to the RAP mode from 6 Hz. It is noted that instability is observed with growing high-frequency oscillations in all three loops. Thereafter, the proposed AD is activated at $t = 22$ s, where these oscillations are suppressed. Fig. 20 demonstrates that the instability originates from the LCL resonance rather than low-frequency interactions. Meanwhile, RAP control will influence the resonance stability, where a larger RAP control bandwidth deteriorates stability.

Another scenario is tested with L_g increased to 0.62 p.u., where the results are shown in Fig. 21. To ensure a stable operation, k_q is initially reduced to 2. As observed, when k_q is restored to its original value of 4 at $t = 5$ s, the system does not remain stable, exhibiting high-frequency oscillations. This confirms that a larger L_g (i.e., a weaker grid) deteriorates the resonance stability of the SL-GFM converter. In contrast, when the proposed AD control is applied, the oscillations are effectively suppressed. Both Fig. 20 and 21 demonstrate that the designed AD control is robust to variations in RAP bandwidth and grid strength.

VI. CONCLUSION

This paper investigates the LCL resonance and AD in SL-GFM converters, mainly with droop-I control, through detailed small-signal analysis. The following conclusions can be drawn:

1) The SL-GFM converter may become an open-loop non-minimum phase system with unstable poles associated with LCL resonance. Therefore, LCL resonance can significantly impact the system closed-loop stability and cannot be simply ignored, even when the resonant frequency is much higher than that of the power loops.

2) When such unstable poles are present, the stability properties associated with the LCL resonance are not decoupled with the low-frequency power loops, with RAP-voltage control playing an important role. A faster RAP loop usually worsens the stability properties of resonance modes. Notably, among various strategies, pure droop-based RAP-voltage control alone cannot ensure stability of the resonance modes.
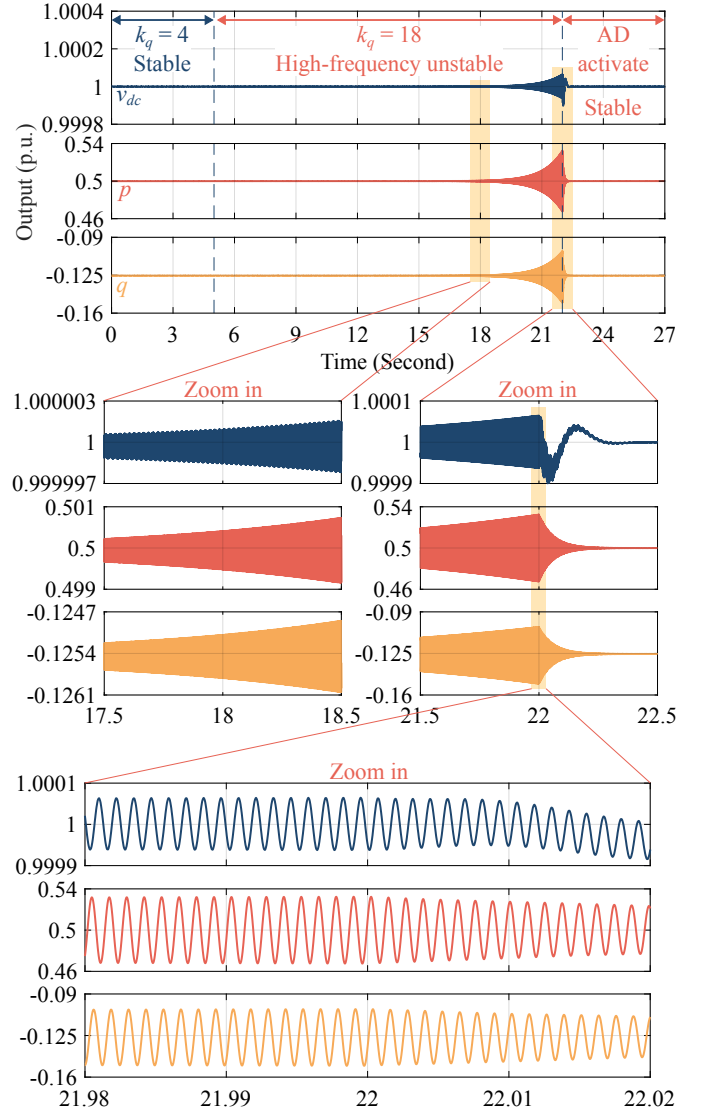

Fig. 20. Simulation results with parameters in Table I.

3) Unlike with GFL converters, where the primary concern is the LCL resonant frequency, SL-GFM converters exhibit distinct resonance stability characteristics. Although the inverter-side and grid-side inductors equally determine the LCL resonant frequency, they play different roles for the stability properties of the resonance modes of the SL-GFM converter. Notably, a larger L_g deteriorates such stability characteristics, constraining the stable operation regime of the SL-GFM converter in a weak grid.

4) In contrast to GFL converters, which typically employ AD via current feedback, SL-GFM converters have improved stability properties when using AD based on capacitor voltage feedback. A worst-case scenario can be defined to facilitate a robust design for AD strategy.

REFERENCES

[1] M. Chen, D. Zhou, A. Tayyebi, E. Prieto-Araujo, F. Dörfler, and F. Blaabjerg, "On power control of grid-forming converters: Modeling,
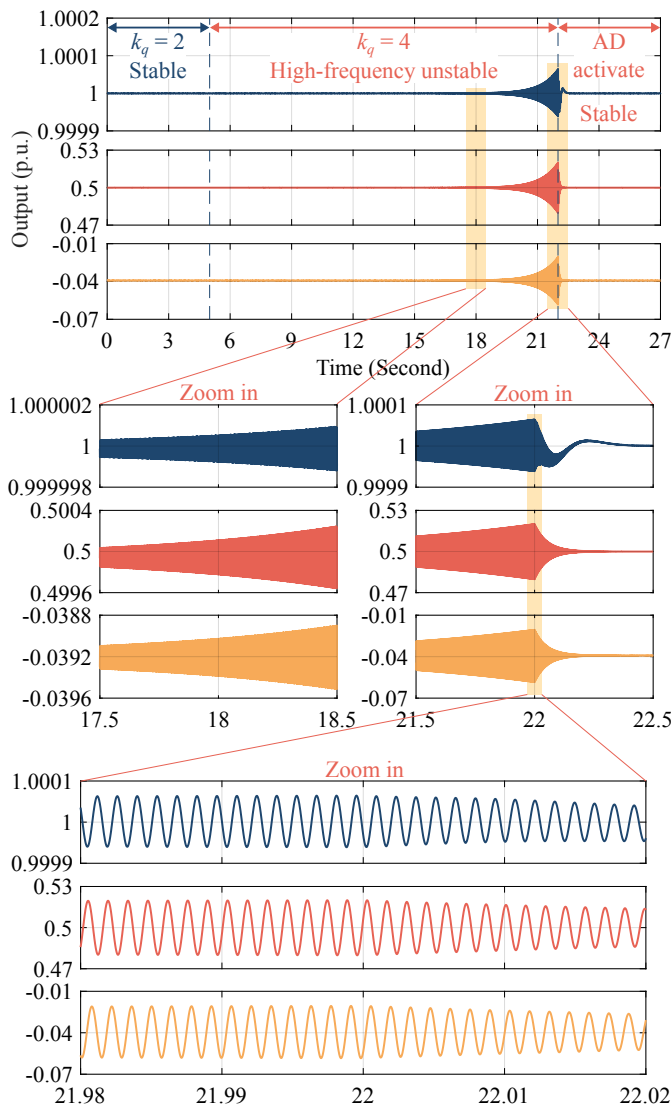
Fig. 21. Simulation results with $L_g = 0.62$ p.u.

based distributed generators," *IEEE Trans. Power Electron.*, vol. 31, no. 5, pp. 3600–3611, May 2016.

[9] W. Du, Z. Chen, K. P. Schneider, R. H. Lasseter, S. Pushpak Nandanoori, F. K. Tuffner, and S. Kundu, "A comparative study of two widely used grid-forming droop controls on microgrid small-signal stability," *IEEE Trans. Emerg. Sel. Topics Power Electron.*, vol. 8, no. 2, pp. 963–975, Jun. 2020.

[10] L. Huang, H. Xin, and F. Dörfler, "H_∞-control of grid-connected converters: Design, objectives and decentralized stability certificates," *IEEE Trans. Smart Grid*, vol. 11, no. 5, pp. 3805–3816, Sep. 2020.

[11] M. Chen, D. Zhou, A. Tayyebi, E. Prieto-Araujo, F. Dörfler, and F. Blaabjerg, "Generalized multivariable grid-forming control design for power converters," *IEEE Trans. Smart Grid*, vol. 13, no. 4, pp. 2873–2885, Jul. 2022.

[12] P. Wang, J. Ma, R. Zhang, S. Wang, T. Liu, and Y. Yang, "Stability criterion for near-area grid-forming converters under the weak grid condition," *IEEE Trans. Power Electron.*, vol. 40, no. 1, pp. 361–374, Jan. 2025.

[13] H. Wu, X. Ruan, D. Yang, X. Chen, W. Zhao, Z. Lv, and Q.-C. Zhong, "Small-signal modeling and parameters design for virtual synchronous generators," *IEEE Trans. Ind. Electron.*, vol. 63, no. 7, pp. 4292–4303, Jul. 2016.

[14] R. Rosso, X. Wang, M. Liserre, X. Lu, and S. Engelken, "Grid-forming converters: Control approaches, grid-synchronization, and future trends—A review," *IEEE Open J. Ind. Appl.*, vol. 2, pp. 93–109, May 2021.

[15] Y. Gu and T. C. Green, "Power system stability with a high penetration of inverter-based resources," *Proc. IEEE*, vol. 111, no. 7, pp. 832–853, Jul. 2023.

[16] D. B. Rathnayake and B. Bahrani, "Multivariable control design for grid-forming inverters with decoupled active and reactive power loops," *IEEE Trans. Power Electron.*, vol. 38, no. 2, pp. 1635–1649, Feb. 2023.

[17] J. Chen and T. O'Donnell, "Parameter constraints for virtual synchronous generator considering stability," *IEEE Trans. Power Syst.*, vol. 34, no. 3, pp. 2479–2481, May 2019.

[18] X. Xiong, Y. Zhou, B. Luo, P. Cheng, and F. Blaabjerg, "Analysis and suppression strategy of synchronous frequency resonance for grid-connected converters with power-synchronous control method," *IEEE Trans. Power Electron.*, vol. 38, no. 6, pp. 6945–6955, Jun. 2023.

[19] H. Deng, J. Fang, Y. Qi, Y. Tang, and V. Debusschere, "A generic voltage control for grid-forming converters with improved power loop dynamics," *IEEE Trans. Ind. Electron.*, vol. 70, no. 4, pp. 3933–3943, Apr. 2023.

[20] S. Jayalath and M. Hanif, "Generalized LCL-filter design algorithm for grid-connected voltage-source inverter," *IEEE Trans. Ind. Electron.*, vol. 64, no. 3, pp. 1905–1915, Mar. 2017.

[21] X. Wang, Y. He, D. Pan, H. Zhang, Y. Ma, and X. Ruan, "Passivity enhancement for LCL-filtered inverter with grid current control and capacitor current active damping," *IEEE Trans. Power Electron.*, vol. 37, no. 4, pp. 3801–3812, Apr. 2022.

[22] S. G. Parker, B. P. McGrath, and D. G. Holmes, "Regions of active damping control for LCL filters," *IEEE Trans. Ind. Appl.*, vol. 50, no. 1, pp. 424–432, Jan./Feb. 2014.

[23] X. Wang, F. Blaabjerg, and P. C. Loh, "Grid-current-feedback active damping for LCL resonance in grid-connected voltage-source converters," *IEEE Trans. Power Electron.*, vol. 31, no. 1, pp. 213–223, Jan. 2016.

[24] T. Liu, J. Liu, Z. Liu, and Z. Liu, "A study of virtual resistor-based active damping alternatives for LCL resonance in grid-connected voltage source inverters," *IEEE Trans. Power Electron.*, vol. 35, no. 1, pp. 247–262, Jan. 2020.

[25] M. Chen, D. Zhou, and F. Blaabjerg, "High penetration of inverter-based power sources with VSG control impact on electromechanical oscillation of power system," *Int. J. Electr. Power Energy Syst.*, vol. 142, pp. 1–12, Jun. 2022.

[26] S. Liu, H. Wu, X. Wang, T. Bosma, and G. Sauba, "Stability analysis and active damping design for grid-forming converters in LC resonant grids," *IEEE Open J. Ind. Electron. Soc.*, vol. 5, pp. 143–154, 2024.

[27] J. Dannehl, F. W. Fuchs, S. Hansen, and P. B. Thøgersen, "Investigation of active damping approaches for pi-based current control of grid-connected pulse width modulation converters with LCL filters," *IEEE Trans. Ind. Appl.*, vol. 46, no. 4, pp. 1509–1517, Jul./Aug. 2010.

[28] M. Chen. [Online]. Available: https://github.com/MengChen-MC/LCLResonanceAnalysis2025

[29] G. F. Franklin, J. D. Powell, and A. Emami-Naeini, *Feedback Control of Dynamic Systems*. Pearson, 2019.

[30] F. Milano, *Power System Modelling and Scripting*. Springer, 2010.

controllability, and full-state feedback design," *IEEE Trans. Sustain. Energy*, vol. 15, no. 1, pp. 68–80, Jan. 2024.

[2] M. Wang and J. V. Milanović, "Simultaneous assessment of multiple aspects of stability of power systems with renewable generation," *IEEE Trans. Power Syst.*, vol. 39, no. 1, pp. 97–106, Jan. 2024.

[3] F. Blaabjerg, M. Chen, and L. Huang, "Power electronics in wind generation systems," *Nat. Rev. Electr. Eng.*, vol. 1, pp. 234–250, Apr. 2024.

[4] D. Pan, X. Wang, F. Liu, and R. Shi, "Transient stability of voltage-source converters with grid-forming control: A design-oriented study," *IEEE Trans. Emerg. Sel. Topics Power Electron.*, vol. 8, no. 2, pp. 1019–1033, Jun. 2020.

[5] W. Du, F. K. Tuffner, K. P. Schneider, R. H. Lasseter, J. Xie, Z. Chen, and B. Bhattarai, "Modeling of grid-forming and grid-following inverters for dynamic simulation of large-scale distribution systems," *IEEE Trans. Power Del.*, vol. 36, no. 4, pp. 2035–2045, Aug. 2021.

[6] S. Liu, H. Wu, T. Bosma, and X. Wang, "Impact of dc-link voltage control on torsional vibrations in grid-forming pmsg wind turbines," *IEEE Trans. Energy Convers.*, vol. 39, no. 4, pp. 2631–2642, Dec. 2024.

[7] A. Tayyebi, D. Gross, A. Anta, F. Kupzog, and F. Dörfler, "Frequency stability of synchronous machines and grid-forming power converters," *IEEE Trans. Emerg. Sel. Topics Power Electron.*, vol. 8, no. 2, pp. 1004–1018, Jun. 2020.

[8] J. Liu, Y. Miura, and T. Ise, "Comparison of dynamic characteristics between virtual synchronous generator and droop control in inverter-